Earth, Planets and Space

FULL PAPER Open Access

Earthquake triggering model based on normal-stress-dependent Nagata law: application to the 2016 Mie offshore earthquake

Shingo Yoshida[1*], Takuto Maeda[2] and Naoyuki Kato[1]

Abstract

We propose a normal-stress-dependent Nagata law. Nagata et al. (J Geophys Res 117:B02314, 2012) revised the rate- and state-dependent friction law by introducing the shear stress dependence. We further extended the Nagata law by incorporating the normal stress dependence obtained by Linker and Dieterich (J Geophys Res 97:4923–4940, 1992). We performed numerical simulations of earthquake triggering by assuming the extended Nagata law. In the case of repeated earthquakes, we applied dynamic Coulomb failure function (CFF) perturbation due to normal or shear stress changes. CFF perturbation increased the slip velocity after the cessation of perturbation, relative to that of the repeated events without triggering. This leads to dynamic earthquake triggering for certain perturbation amplitudes with time to instability of 0 to several tens of days. In addition, triggering potential of the static CFF jump (ΔCFF_s) was investigated. Static stress perturbation has a higher triggering potential than dynamic stress perturbation for the same magnitude of CFF. The equivalent ΔCFF_{eq} is evaluated for dynamic perturbation that results in a triggering potential approximately the same as in the case of static stress perturbation if $\Delta CFF_s = \Delta CFF_{eq}$. We calculated ΔCFF_{eq} on the interface of the Philippine Sea plate for the Mie offshore earthquake, which occurred around the Nankai Trough on April 1, 2016, using OpenSWPC. The results shows that ΔCFF_{eq} is large around the trough, where slow slip events followed the Mie earthquake, suggesting that a large ΔCFF_{eq} may have triggered slow slip events.

Keywords: Normal-stress-dependent Nagata law, Earthquake triggering, Coulomb stress perturbation, 2016 Mie offshore earthquake, OpenSWPC, Numerical simulation, Slow slip events

Introduction

There have been many reports of earthquake triggering (e.g., Hill et al. 1993; Brodsky et al. 2000; Kilb et al. 2000; Miyazawa et al. 2008; van der Elst and Brodsky 2010; Richards-Dinger et al. 2010; Miyazawa 2011; Parsons and Velasco 2011; Lin 2012; Pollitz et al. 2012; van der Elst et al. 2013; Yukutake et al. 2013; Johnson and Bürgmann 2016; Miyazawa 2016; Uchida et al. 2016; Yoshida 2016). Besides the seismic event triggering, triggering of very low-frequency earthquakes, tremors, slow slip events (SSEs), and creep events has been observed (e.g., Allen et al. 1972; Obara 2009; Itaba and Ando 2011; To et al. 2015; Araki et al. 2017; Miyazawa 2019; Canitano et al. 2019; Katakami et al. 2020). A likely mechanism behind earthquake triggering has been based on the rate- and state-dependent friction (RSF) law (Dieterich 1979; Ruina 1983). Dieterich (1994) obtained the time to instability as a function of slip velocity based on a spring-block model, and found that an increase in the slip velocity due to a static stress change could trigger an earthquake. This model has been extended to include dynamic stress perturbation, which reduces the friction strength (expressed as a state variable), causing an increase in slip velocity (e.g., Yoshida 2018).

Numerical simulations of dynamic triggering have been extensively performed by Gomberg et al. (1997, 1998), Belardinelli et al. (2003), Savage and Marone (2008), and van der Elst and Savage (2015) using a spring-block

*Correspondence: shingo@eri.u-tokyo.ac.jp
[1] Earthquake Research Institute, University of Tokyo, Tokyo, Japan
Full list of author information is available at the end of the article

model, and by Perfettini et al. (2003), and Kaneko and Lapusta (2008) using a one-dimensional (1D) fault in a two-dimensional (2D) medium in the RSF framework. Besides the seismic event simulation, Du et al. (2003), Perfettini and Ampuero (2008), and Wei et al. (2015) performed numerical simulations of triggering of SSEs, assuming velocity weakening region with a system stiffness smaller than but close to a critical value, or velocity strengthening region. Although the slip velocity acceleration after the start of the instability is different between the seismic event and SSEs, the growth of the rupture nucleation leading to the instability is basically the same, and hence, the same triggering mechanism is applicable.

Yoshida (2018) performed numerical simulations of earthquake triggering by assuming a circular asperity that obeys a RSF law revised by Nagata et al. (2012). He also discussed delayed and instantaneous triggering due to changes in dynamic and/or static stress assuming a constant normal stress. In the present study, we will incorporate the normal stress dependence obtained through normal stress jump experiments by Linker and Dieterich (1992) into the Nagata law, and discuss Coulomb stress change (CFF) for this law in "Normal-stress-dependent Nagata law" section. With regard to dynamic stress perturbation, we will define ΔCFF_{eq} so that the triggering potential of the dynamic perturbation is approximately the same as that of the static CFF change if ΔCFF_{eq} is equal to the value of static CFF. In "Simulation of earthquake triggering" section, we perform a numerical simulation of earthquake triggering. In "CFF due to the 2016 Mie offshore earthquakes" section, we will calculate ΔCFF_{eq} on the interface of the Philippine Sea plate due to the Mie offshore earthquake, which occurred around the Nankai Trough on April 1, 2016.

Normal-stress-dependent Nagata law

On the basis of the friction experiments for constant normal stress, Nagata et al. (2012) provided a revised RSF law, which is given as:

$$\frac{\tau}{\sigma} = \mu = \mu^* + a \ln\left(\frac{V}{V^*}\right) + b \ln\left(\frac{\theta}{\theta^*}\right), \tag{1}$$

$$\frac{d\theta}{dt} = 1 - \frac{V}{L}\theta - \frac{c\theta}{b\sigma}\frac{d\tau}{dt}, \tag{2}$$

where τ is the shear stress, σ is the effective normal stress, a and b are friction parameters, L is the characteristic slip, θ is a state variable, V^* is an arbitrarily chosen reference velocity, θ* is a reference state at $V = V^*$, and c is the stress-weakening effect coefficient. The slip law (Ruina 1983) and the aging law (Dieterich 1979) are used most frequently in numerical simulations. However, the former cannot reproduce the log t healing at zero slip velocity, and the latter cannot represent symmetric stress changes for sudden increases and decreases of the slip velocity. The Nagata law can reproduce both of these behaviors found in the laboratory experiments. As $\tau = \mu\sigma$, Eq. (2) may be written as:

$$\frac{d\theta}{dt} = 1 - \frac{V}{L}\theta - \frac{c\mu\theta}{b\sigma}\frac{d\sigma}{dt} - \frac{c\theta}{b}\frac{d\mu}{dt}, \tag{3}$$

which apparently represents normal stress dependence. However, Eq. (2) was derived from the experimental data for constant normal stress, so that the third term $\frac{c\mu\theta}{b\sigma}\frac{d\sigma}{dt}$ on the right-hand side of Eq. (3) was not experimentally confirmed.

Linker and Dieterich (1992) conducted normal stress step experiments, keeping constant sip velocity V, and proposed the following evolution law that considers the effect of variable normal stress:

$$\frac{d\theta}{dt} = 1 - \frac{V}{L}\theta - \frac{\alpha\theta}{b\sigma}\frac{d\sigma}{dt}, \tag{4}$$

where α is a constitutive parameter representing normal stress dependence. Incorporating the third term of Eq. (4) to Eq. (2), we propose the following normal-stress-dependent Nagata law as:

$$\frac{d\theta}{dt} = 1 - \frac{V}{L}\theta - \frac{\alpha\theta}{b\sigma}\frac{d\sigma}{dt} - \frac{c\theta}{b}\frac{d\mu}{dt}, \tag{5}$$

which includes laboratory-derived normal and shear stress dependences. Although Eq. (3) can be regarded as a specified version of Eq. (5) for $\alpha = c\mu$, since Nagata et al. (2012) derived Eq. (2) on the basis of a laboratory experiment under the constant normal stress, they did not check whether the normal stress change followed $\frac{c\mu\theta}{b\sigma}\frac{d\sigma}{dt}$ or not.

From Eq. (5) and the time derivative of Eq. (1), we obtain:

$$\frac{d\mu}{dt} = a\frac{d\ln\left(\frac{V}{V^*}\right)}{dt} + \frac{b}{\theta}\left(1 - \frac{V}{L}\theta - \frac{\alpha\theta}{b\sigma}\frac{d\sigma}{dt} - \frac{c\theta}{b}\frac{d\mu}{dt}\right). \tag{6}$$

Inserting $\frac{d\mu}{dt} = \frac{1}{\sigma}\left(\frac{d\tau}{dt} - \mu\frac{d\sigma}{dt}\right)$ into Eq. (6), we obtain:

$$\frac{d\ln(V/V^*)}{dt} = \frac{1}{a\sigma/(1+c)}\left\{\frac{d\tau}{dt} - \left(\mu - \frac{\alpha}{1+c}\right)\frac{d\sigma}{dt}\right\} - \frac{b}{a}\left(\frac{1}{\theta} - \frac{V}{L}\right). \tag{7}$$

Linker and Dieterich (1992) performed normal stress step tests where the normal stress was suddenly changed from σ_0 to $\sigma_1 = \sigma_0 + \Delta\sigma$ keeping the constant sliding

velocity. In such a case, the change in $\ln(V/V^*)$ due to the normal stress jump is written as:

$$\Delta \ln\left(V/V^*\right) = \frac{1}{a\sigma/(1+c)}\Delta\mathrm{CFF} - \frac{b}{a}\int_0^{\Delta t}\left(\frac{1}{\theta} - \frac{V}{L}\right)\mathrm{d}t, \tag{8}$$

where

$$\Delta\mathrm{CFF} = \Delta\tau - \left(\mu - \frac{\alpha}{1+c}\right)\Delta\sigma. \tag{9}$$

Equation (9) defines ΔCFF for the extended Nagata law, which coincides with usual ΔCFF when $\alpha = c = 0$. The left-hand side of Eq. (8) is zero because of the constant V, and the second term on the right-hand side is approximately zero because Δt takes a very small value and θ has a steady-state value of L/V immediately before the normal stress jump so that ΔCFF is also approximately zero. Therefore, the increase of the shear stress is written as:

$$\Delta\tau = \left(\mu - \frac{\alpha}{1+c}\right)\Delta\sigma. \tag{10}$$

Linker and Dieterich (1992) defined $\delta_L\tau$ as the difference between the stress immediately after the stress jump and the following steady-state stress, as shown in Fig. 1a. For the case of the normal-stress-dependent Nagata law, Eq. (10) leads to

$$\delta_L\tau = \left(\frac{\alpha}{1+c}\right)\Delta\sigma. \tag{11}$$

Linker and Dieterich (1992) found that $\delta_L\mu = \delta_L\tau/\sigma$ changes as follows:

$$\delta_L\mu = \alpha\ln\left(\frac{\sigma+\Delta\sigma}{\sigma}\right) \approx \alpha\frac{\Delta\sigma}{\sigma}. \tag{12}$$

Comparing Eqs. (11) and (12), scaling relation for α between the normal stress-dependent aging law and the Nagata law is represented as:

$$\frac{\alpha}{1+c}|_{\mathrm{Nagata}} = \alpha|_{\mathrm{aging}}. \tag{13}$$

Figure 1a shows the simulation result of the normal stress step test from $\sigma_0 = 5$ MPa to $\sigma_1 = 6$ MPa using the 1D spring-block model for the aging law (4). The assumed parameters are $a = 0.012$, $a-b = -0.0015$, $L = 2.25\times10^{-6}$ m, $\alpha = 0.2$, and $V = 1\times10^{-6}$ m/s. Figure 1b shows the result when assuming the normal stress-dependent Nagata law (5). To reproduce the change in the same way as the aging law, the following scaling relationships were given by Bhattacharya and Rubin (2014) as:

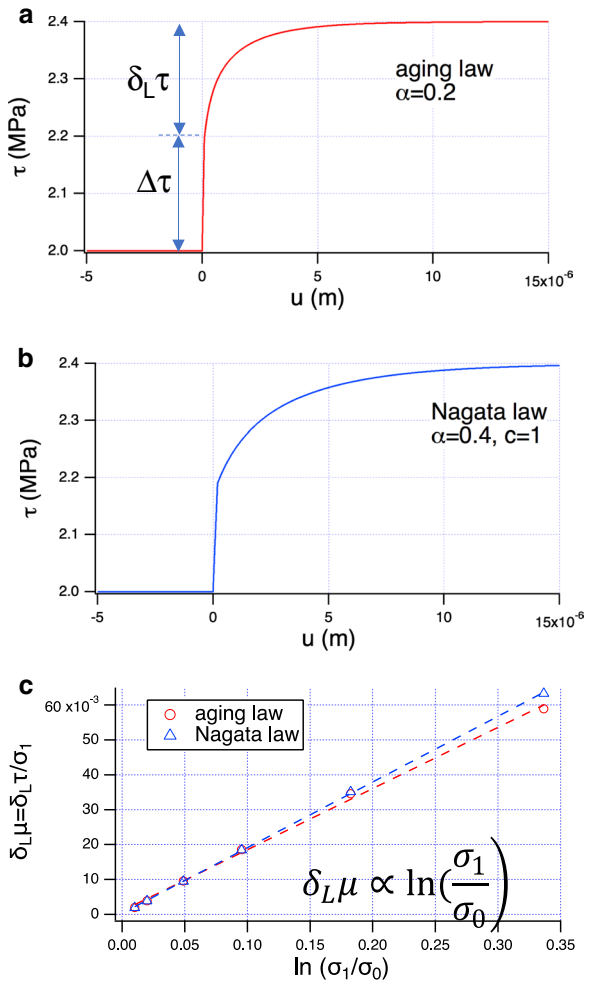

Fig. 1 Simulation of the normal stress step test. During stable sliding at a constant velocity, we applied static normal stress change $\sigma_0 = 5$ MPa to $\sigma_1 = 6$ MPa. **a** Shear stress change assuming the aging law. $a = 0.012$, $a-b = -0.0015$, $L = 2.25\times10^{-6}$ m, and $\alpha = 0.2$. **b** Shear stress change assuming the normal-stress-dependent Nagata law. The friction parameters were converted using the scaling relations (14) and (15) with $c = 1$. **c** The relationship between $\delta_L\mu$ and $\ln(\sigma_1/\sigma_0)$ for the aging law and the Nagata law

$$\begin{aligned}
&\frac{a}{1+c}|_{\mathrm{Nagata}} = a|_{\mathrm{aging}},\\
&(a-b)|_{\mathrm{Nagata}} = (a-b)|_{\mathrm{aging}},\\
&L\{1 - c(a-b)/b\}|_{\mathrm{Nagata}} = L|_{\mathrm{aging}}.
\end{aligned} \tag{14}$$

The friction parameters were converted using the scaling relationships (13) and (14) with $c = 1$. The shear stress for the Nagata law changes in a similar way as that for the aging law. Figure 1c shows the simulated relationship between $\delta_L\mu$ and $\ln(\sigma_1/\sigma_0)$ for the aging law and

the Nagata law. Indeed, the Nagata law with the scaling relationships reproduces frictional changes similar to those derived from the aging law. In these simulations, we assumed a very high stiffness of the slider to keep the sliding velocity constant at the time of the sudden normal stress change, while Linker and Dieterich (1992) suddenly changed the normal stress keeping a constant sliding velocity using a servo-controlled system.

It is noted that when $\alpha = 0$, the shear stress reaches a steady-state value instantaneously at the time of the normal stress change. This means that when α is smaller, the shear stress is more sensitive to the normal stress change. On the basis of the assumption that the shear stress is proportional to the true contact area (e.g., Nakatani, 2001), when the normal stress doubles, the contact area becomes twice as large instantaneously if $\alpha = 0$.

Simulation of earthquake triggering

We use the same model as that by Kato (2004), and Yoshida (2018), who describe the simulation process in detail. A 2D planar fault is loaded at a constant rate V_{pl} in the x-direction, and the fault plane is divided into 256×256 square cells with areas of 0.5 km $\times$ 0.5 km. The shear stress τ on cell (i, j) is given by:

$$\tau(i,j) = \sum_{k,l} K(i-k, j-l)\left[u(k,l) - V_{pl}t\right] - \frac{G}{2\beta}V(i,j), \tag{15}$$

where $u(k, l)$ is the slip at cell (k, l) in the x-direction, $K(i-k, j-l)$ is the static shear stress at the center of cell (i, j) due to the uniform unit slip in the x-direction over cell (k, l), $V = \mathrm{d}u/\mathrm{d}t$ is the slip velocity, G is the rigidity, and β is the S wave speed. In all of our simulations, we assumed that $V_{pl} = 0.085$ m/year, $G = 30$ GPa, and $\beta = 3.5$ km/s. The second term on the right-hand side of Eq. (15) represents the approximate reduction in shear stress due to wave radiation, as introduced by Rice (1993).

We first simulate the unperturbed earthquake cycle using constitutive law (1), normal stress-dependent Nagata law (5), and Eq. (15). Assuming $a = 0.03$, $a-b = -0.012$ and 0.0014 (inside and outside the asperity of radius $R = 3$ km, respectively), $\sigma = 50$ MPa, $L = 0.003$ m, $\alpha = 4.2$, and $c = 20$, we obtained the earthquake cycle shown in Fig. 2. Earthquakes occur repeatedly with a recurrence interval $T_r = 20$ years. Bhattacharya et al. (2015) estimated the value of c at 10 to 100 based on laboratory experiments using a rock interface with gouge, which is larger than the value of 2 estimated by Nagata et al. (2012) from bare rock experiments. We obtain $\alpha = 4.2$ using the scaling relationship with $\alpha = 0.2$ for the aging law and $c = 20$. In this section, we apply Coulomb stress perturbations of various

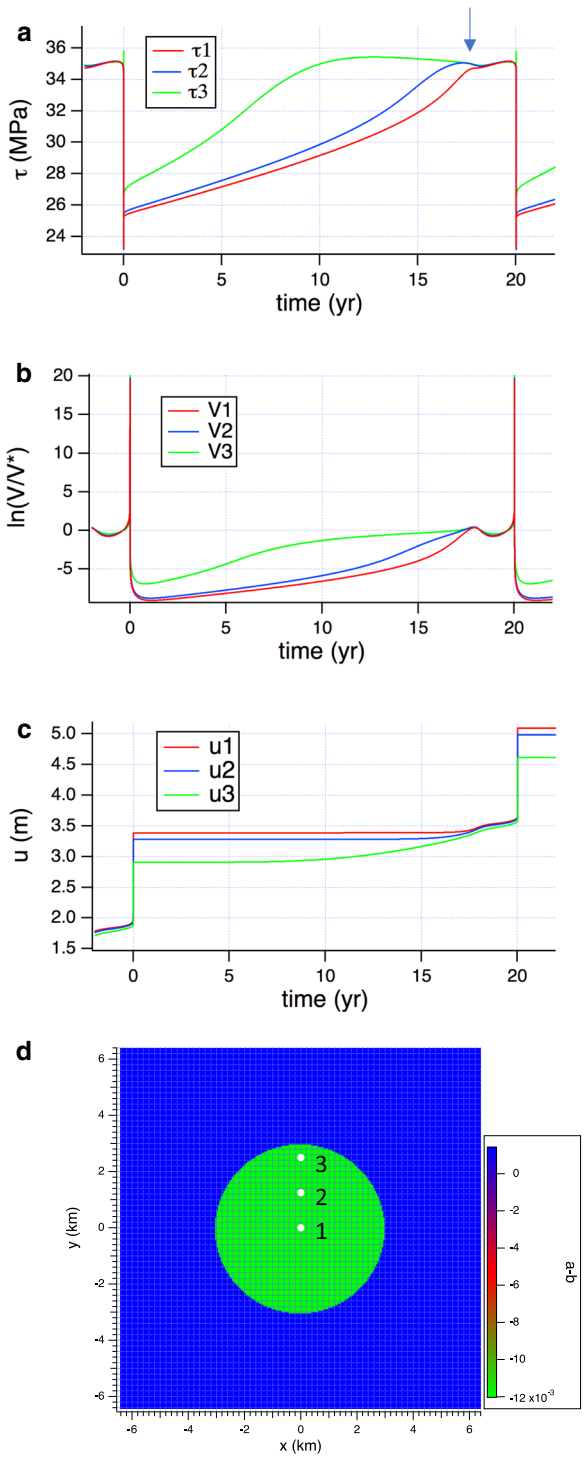

Fig. 2 Simulation of earthquake cycle. **a** Change in shear stresses. Stress perturbation will be applied at the timing indicated by the arrow. **b** Change in slip velocities on a log scale. **c** Change in displacements. **d** Distribution of $a-b$. The three white dots denote the points at which the histories are shown. The suffixes in a to c correspond to the points. The assumed parameters are $a = 0.03$, $a-b = -0.012$ and 0.0014 (inside and outside the asperity, respectively), $\sigma = 50$ MPa, $L = 0.003$ m, $\alpha = 4.2$, and $c = 20$

amplitudes assuming the same friction parameters. Figure 2 shows the evolution of the shear stresses and slip velocities on a log scale, and that of the displacements at the three points indicated in Fig. 2d.

Next, we apply dynamic shear and/or normal stress perturbation:

$$\begin{aligned} \tau_d(t) &= S_d \sin\left(\frac{2\pi}{T_p}t\right), \\ \sigma_d(t) &= N_d \sin\left(\frac{2\pi}{T_p}t\right) \quad 0 \le t \le T_p. \end{aligned} \tag{16}$$

The corresponding dynamic Coulomb stress perturbation $\mathrm{CFF}_d(t)$ is

$$\mathrm{CFF}_d(t) = \Delta\mathrm{CFF}_d \sin\left(\frac{2\pi}{T_p}t\right), \quad 0 \le t \le T_p, \tag{17}$$

with

$$\Delta\mathrm{CFF}_d = S_d - \left(\mu - \frac{\alpha}{1+c}\right)N_d, \tag{18}$$

where S_d and N_d are the amplitude of the shear and normal stress perturbation, respectively, T_p is the period and $t=0$ is taken to be the time when the perturbation is applied.

Figure 3a shows the Coulomb stress perturbation applied at 7/8 of the recurrence interval $T_r \sim 20$ years, as indicated with the arrow in Fig. 2a. The assumed parameters are $S_\mathrm{d}=0$ MPa, $N_\mathrm{d}=-1.48$ MPa, $\mu=0.7$, $\alpha=4.2$, $c=20$, and $T_p=100$ s. Figure 3b, c shows the slip velocity and displacement, respectively, at the three points in the asperity shown in Fig. 2d.

Dieterich (1994) represented the time to instability as a function of slip velocity using a single spring-block model and pointed out that an increase in the slip velocity due to a static stress change could trigger an earthquake. This model can be extended to incorporate dynamic stress perturbation, which reduces the frictional strength, causing an increase in slip velocity. Figure 3b shows that the slip velocity after the perturbation ceased is higher than that before the perturbation starts.

Figure 4 shows that the slip accelerates after the perturbation starts at $t=0$, with the triggered event occurring approximately 17.4 days later. The increase in slip velocity promotes the rupture nucleation growth, resulting in the reduction of the time to instability from 2.5 year to 17.4 days.

Figure 5a shows the relationship between the amplitudes of the stress perturbation and the time to instability. The values of the friction parameters are the same as those in Fig. 2. The red circles show the effects of the shear stress change without normal stress perturbation ($N_\mathrm{d}=0$), and the other circles represent the effects of the normal stress changes with $S_\mathrm{d}=0$. The assumed values of α are 0 (orange), 2.1 (green), and 4.2 (black), respectively.

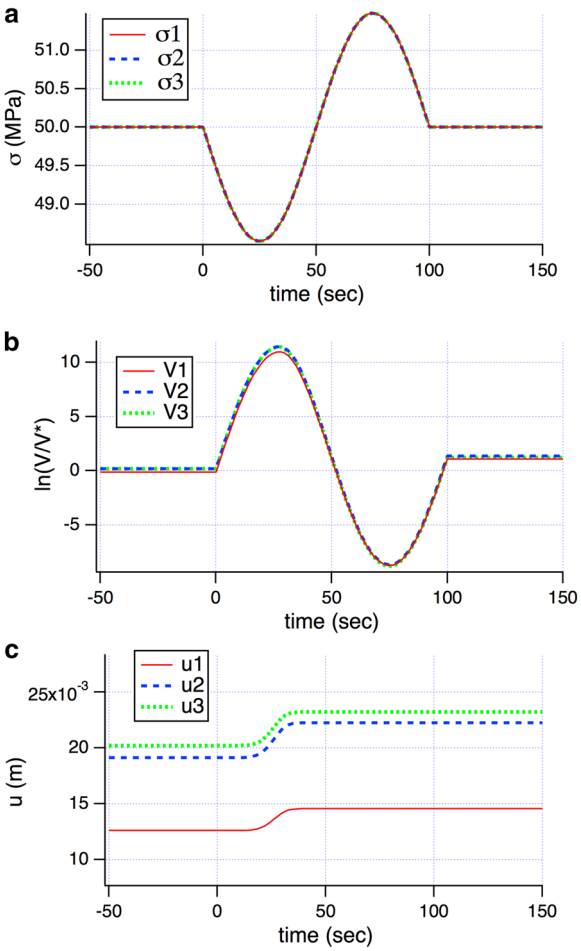

Fig. 3 **a** Changes in the normal stress at the three points denoted in Fig. 2d. **b** Slip velocities on a log scale. **c** Displacements. Here, $t=0$ is taken as the time when the normal stress perturbation of $N_d=-1.48$ MPa is applied. The timing is shown by the arrow in Fig. 2a. The friction parameters are the same as those in Fig. 2

The time to instability decreases, i.e., the triggering potential is high, as the stress amplitude increases. As small values of α results in large values of $\Delta\mathrm{CFF}_\mathrm{d}$ for negative N_d as denoted by Eq. (18), the values of N_d required to cause a certain time to instability decrease when α is small. The relationships of $\Delta\mathrm{CFF}_\mathrm{d}$ calculated using Eq. (18) and the time to instability are plotted in Fig. 5b, which shows that the curves for the four cases closely overlap. This means that the triggering potential is determined mainly by a value of $\Delta\mathrm{CFF}_\mathrm{d}$.

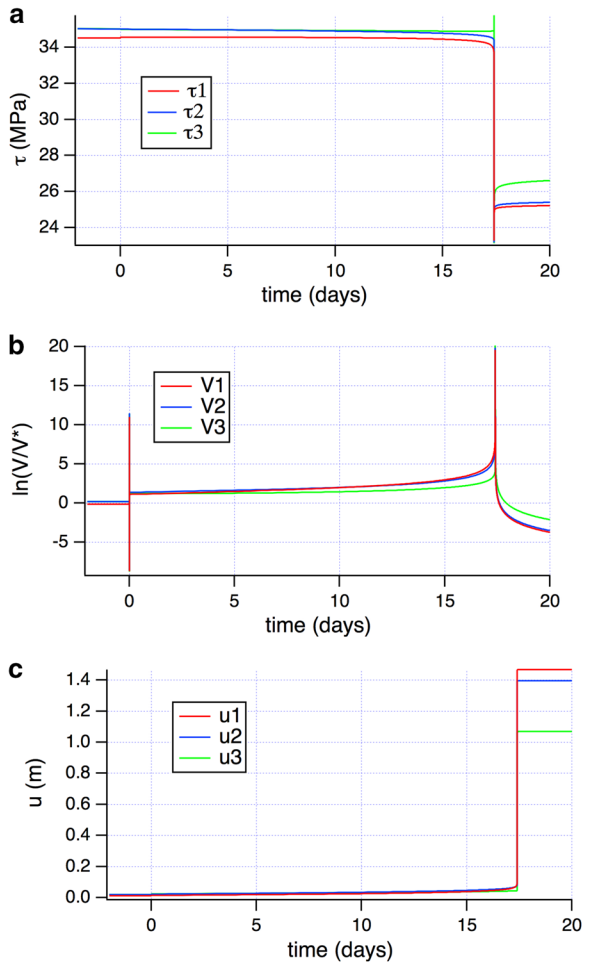

Fig. 4 **a** Changes in the shear stresses at the three points denoted in Fig. 2d including the period during the triggering perturbation (shown by the expanded time axes in Fig. 3), the following period, and the triggered instability. **b** Changes in velocities. **c** Changes in displacements. The parameters are the same as those in Fig. 2. Figure 3 shows expansions of these plots around $t=0$

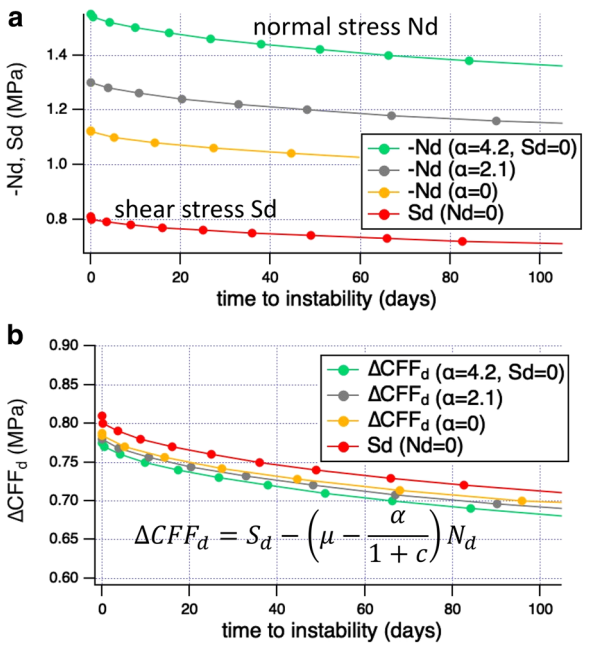

Fig. 5 **a** Relationship of the dynamic stress perturbation amplitude and the time to instability. The values of the friction parameters are the same as those in Fig. 2. The red circles show the effects of the shear stress change, and the other circles represent the effects of the normal stress changes. The assumed values for α are 0 (orange), 2.1 (green), and 4.2 (black), respectively. **b** Relationship of ΔCFF_d and the time to instability

Triggering by static stress change is also simulated. At $t=0$, static stress jump is applied:

$$\begin{aligned} \tau_s(t) &= S_s t/T_p \quad 0 \le t \le T_p \\ &= S_s \quad t > T_p \\ \sigma_s(t) &= N_s t/T_p \quad 0 \le t \le T_p \\ &= N_s \quad t > T_p \end{aligned} \tag{19}$$

The corresponding Coulomb stress jump is written as

$$\begin{aligned} \mathrm{CFF}_s(t) &= \Delta\mathrm{CFF}_s t/T_p \quad 0 \le t \le T_p \\ &= \Delta\mathrm{CFF}_s \quad t > T_p, \end{aligned} \tag{20}$$

with

$$\Delta\mathrm{CFF}_s = S_s - \left(\mu - \frac{\alpha}{1+c}\right) N_s. \tag{21}$$

Figure 6a shows the effect of the static stress changes S_s and N_s on the time to instability by assuming $\mu=0.7$, $\alpha=4.2$, $c=20$, and the same friction parameters as in Fig. 2a. Figure 6b shows the relationship between $\Delta\mathrm{CFF}_s$ and the time to instability. The two curves for the shear and normal stress jumps completely overlap. In the static case the triggering potential is a function of $\Delta\mathrm{CFF}_s$.

Dieterich et al. (2000) pointed out that a modified Coulomb stress change based on conventional RSF for static triggering is given by $\Delta\mathrm{CFF}_m = S_s - (\mu - \alpha) N_s$. If scaling relationship (13) is satisfied, $\Delta\mathrm{CFF}_m$ takes the same value as $\Delta\mathrm{CFF}_S$ evaluated using Eq. (21) for given S_s and N_s.

The change $\Delta_s \ln(V/V^*)$ due to the static jump of CFF can be approximately obtained using Eq. (7),

$$\Delta_S \ln(V/V^*) = \frac{\Delta\mathrm{CFF}_s}{a\sigma/(1+c)}. \tag{22}$$

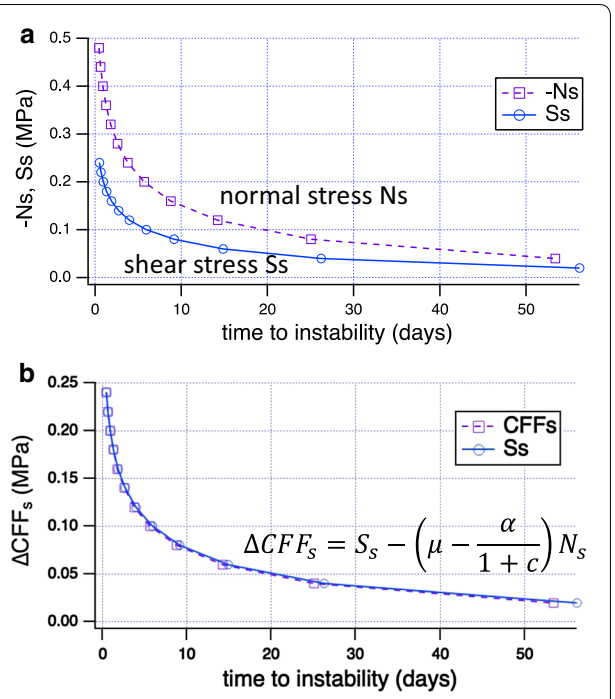

Fig. 6 **a** Relationship of the static stress perturbation amplitude and the time to instability: only shear stress changes are assumed (blue circles), and only the normal stress changes are assumed (the purple squares). **b** Relationship between ΔCFF_s and the time to instability

Note that in the previous section, we derived some equations under the condition of $V=$ const. to reproduce the experimental results obtained by Linker and Dieterich (1992). As V is not controlled in the earthquake cycle simulations, $\ln V$ increases in proportional to ΔCFF_S.

Comparing Figs. 5b and 6b, we find that values of ΔCFF_s for static change smaller than ΔCFF_d for dynamic change can trigger instability. This means that a value of ΔCFF itself cannot be used for evaluating the triggering potential to compare the static and dynamic perturbations. This is consistent with previous observations. For instance, Kilb et al. (2000) reported that the aftershocks of the 1992 Landers earthquake (M7.3) were possibly triggered not only by static stress changes, but also by dynamic stress changes with much larger amplitude than that of the static changes. In the case of dynamic triggering, the applied Coulomb stress becomes zero after the perturbation ceases, as implied by Eq. (19), and ΔCFF_d makes no direct contribution to the first term of the right-hand side of Eq. (7) for changing $\Delta\ln(V/V^*)$.

Next, we consider the increases of V when the following dynamic perturbation $CFF_d(t)$:

$$\begin{aligned} CFF_d(t) &= \tau_d(t) - \left(\mu - \frac{\alpha}{1+c}\right)\sigma_d(t) \quad 0 < t < T_n \\ &= 0 \quad t > T_n. \end{aligned} \tag{23}$$

The velocity when the perturbation is applied, based on Eq. (7), is approximately

$$\ln\left(V_d(t)/V_i\right) = \frac{CFF_d(t)}{a\sigma/(1+c)}, \tag{24}$$

or

$$V_d(t) = V_i \exp\left[\frac{CFF_d(t)}{a\sigma/(1+c)}\right], \tag{24b}$$

where V_i is the velocity just before applying the perturbation. The displacement during the perturbation is given by

$$\Delta u = \int_0^{T_n} V_d \mathrm{d}t. \tag{25}$$

As $CFF_d(t)=0$ after the perturbation ceases, Eq. (8) approximately leads to

$$\Delta \ln(V/V^*) = \frac{b}{aL}\Delta u = \frac{b}{aL}\int_0^{T_n} V_d(t)\mathrm{d}t. \tag{26}$$

Here, we ignored the integral of $1/\theta$ in Eq. (8) because the values were less than 5% of values estimated using the right-hand side of Eq. (26) in the numerical simulations in Fig. 5. Moreover, $\Delta\tau$ has a small value after the perturbation because of the displacement. Heterogeneous displacement inside the asperity can cause both stress release and stress concentration depending on location and heterogeneity.

We evaluate the equivalent ΔCFF_{eq} for the dynamic perturbation, which results in the same velocity increase as that obtained in the case of static stress perturbation when $\Delta CFF_s = \Delta CFF_{eq}$. Comparing Eqs. (22) and (26), ΔCFF_{eq} is represented by

$$\begin{aligned} \Delta CFF_{eq} &= \frac{b\sigma}{L(1+c)}\int_0^{T_n} V_d(t)\mathrm{d}t, \\ &= \frac{b\sigma V_i}{L(1+c)}\int_0^{T_n} \exp\left[\frac{CFF_d(t)}{a\sigma/(1+c)}\right]\mathrm{d}t. \end{aligned} \tag{27}$$

ΔCFF_{eq} is independent of a value of c including $c=0$ (aging law) when the scaling relations (13) and (14) are satisfied. Figure 7 shows ΔCFF_{eq} using the average velocity over the asperity before the perturbation starts as V_i. It is found that the triggering potentials for the dynamic and static perturbations are similar when $\Delta CFF_s = \Delta CFF_{eq}$.

Effects of stress perturbation timing were briefly discussed by Yoshida (2018) assuming constant normal

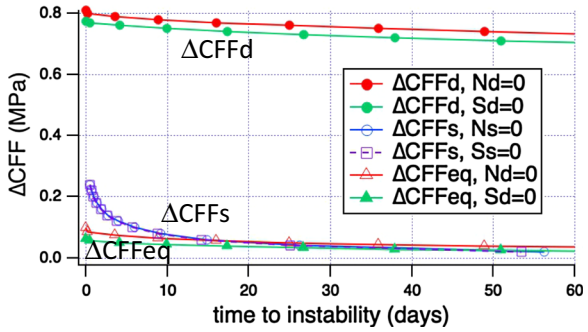

Fig. 7 Relationship between CFF and the time to instability. The red, green, and blue circles, and the purple squares are the same as those plotted in Figs. 5b and 6b. In addition, ΔCFF_{eq} for the shear stress change only, and the normal stress change only are plotted

stress. As the effects of timing may not be changed essentially by including the normal stress dependence, we do not discuss this subject here.

CFF due to the 2016 Mie offshore earthquakes

In this section, we will calculate ΔCFF_{eq} using Eq. (27) for the Mie offshore earthquake which occurred around the Nankai Trough on April 1, 2016. Takemura et al. (2018) obtained the moment tensor of this earthquake by inversion analysis using the broadband records from the full-range seismograph network (F-net) stations. The inversion solution was dip = 20°, strike = 250°, rake = 110°, and $M_w = 5.9$.

Maeda et al. (2017) developed an open-source integrated parallel simulation code (OpenSWPC) for modeling seismic wave propagation in 3D heterogeneous viscoelastic media. In this paper, we updated OpenSWPC to calculate a stress tensor. We obtain the stress field for the 2016 Mie offshore earthquake using the modified code, assuming a point source with the moment tensor obtained by Takemura et al. (2018) and Japan Integrated Velocity Structure Model (Koketsu et al. 2012).

We calculate Coulomb stresses at grid points with intervals of 10 km on the interface of oceanic layer 2 (basement) of the Philippine Sea Plate. The point adjacent to the epicenter of the Mie offshore earthquake, which is denoted by a star symbol in Fig. 8, is excluded because the point source approximation is not applicable. The total number of the grid points is 15 × 13-1. The point adjacent to the epicenter of the Mie offshore earthquake, which is denoted by a star symbol in Fig. 8, is excluded because the point source approximation is not applicable. The assumed mechanism of the target fault is dip = 15°, strike = 240°, and rake = 110°, which are the same as those Satake (1993) assumed for the 1944 Tonankai earthquake. Figure 9a, b shows shear stress $\tau_d(t)$ and normal stress $\sigma_d(t)$, respectively, calculated at point A shown in Fig. 8c.

Nagata et al. (2012) obtained $c = 2$ through a laboratory experiment, and Linker and Dieterich (1992) obtained $\alpha = 0.2$ for the aging law. Using these values, the scaling relationship (13) leads to $\alpha = 0.6$ for the Nagata law. Figure 9 (c) shows $CFF_d(t)$ based on Eq. (23) by assuming these values and $\mu = 0.6$. We calculated $CFF_d(t)$ from the occurrence time $t = 0$ to 450 s (the latter part is not shown in Fig. 9), and we obtained ΔCFF_s by averaging $CFF_d(t)$ from 400 s to 450 s when the most of oscillations vanishes. Figure 8a, b shows the distributions of the maximum value CFF_{d_max} of $CFF_d(t)$ and ΔCFF_s, respectively. CFF_{d_max} and ΔCFF_s have large values near the hypocenter with largest values of 310 kPa and 38 kPa, respectively, at point A shown in Fig. 8c.

Next, we obtain ΔCFF_{eq} from $CFF_d(t)$ using Eq. (27), assuming values of many parameters that are not constrained by observations. Hence, we provide an example of evaluation in this paper. The assumed variation with depth, $\gamma = a - b$, is shown in Fig. 10. In the shallow and deep regions, $\gamma_0 = 5.0 \times 10^{-4}$, and in the seismic region, $\gamma_{seis} = -3.0 \times 10^{-4}$. The variation of γ is similar to that in model 4 assumed by Kato and Hirasawa (1999). They performed a numerical simulation of a large earthquake cycle in the Tokai district using the aging law. The other friction parameters for the aging law are assumed to be $a = 5.2 \times 10^{-4}$, $L = 1.0 \times 10^{-2}$ m, and μ = 0.6, and they are independent of depth. The parameters for the Nagata law are determined using the scaling relation (13) with $c = 2$ from the aging law parameters.

The slip velocity V_i just before applying the perturbation is assumed to be $V_{i\_0} = 3.3$ cm/year in both deep and shallow regions with $\gamma_0 = 5.0 \times 10^{-4}$, and $V_{i\_seis} = 0.33$ cm/year in the seismic region with $\gamma_{seis} = -3.0 \times 10^{-4}$. V_i in the other region is assumed to be a linear function of γ, i.e., $V_i = V_{i\_0} + (\gamma - \gamma_0)(V_{i\_seis} - V_{i\_0})/(\gamma_{seis} - \gamma_0)$. We represent pore pressure at depth d using over-pressure rate R_{OP} from 0 to 1 as:

$$P_p(d) = \sigma_H(d) + R_{OP}(\sigma_L(d) - \sigma_H(d)),$$

where $\sigma_H(d)$ and $\sigma_L(d)$ are the hydrostatic and lithostatic pressure, respectively, given by $\sigma_L(d) = \rho g(d - d_{sf}) + \rho_w g d_{sf}$, $\sigma_H(d) = \rho_w g d$, with $\rho = 2.75 \times 10^3$ kg/m^3, $\rho_w = 1.0 \times 10^3$ kg/m^3, $g = 9.8$ m/s^2, and d_{sf} = seafloor depth. The effective normal stress is given as a function of depth by

$\sigma_e(d) = \sigma_L(d) - P_p(d)$.

When R_{OP} is assumed to be 68%, the maximum value of ΔCFF_{eq} at point B is comparable to the maximum value of ΔCFF_s at point A. Figure 8c, d shows the distribution of ΔCFF_{eq} and the effective normal stress, respectively. The ΔCFF_{eq} distribution shows a different pattern than the CFF_{d_max} distribution. For a larger R_{OP}, e.g., for a larger pore pressure, ΔCFF_{eq} becomes larger. As Fig. 11

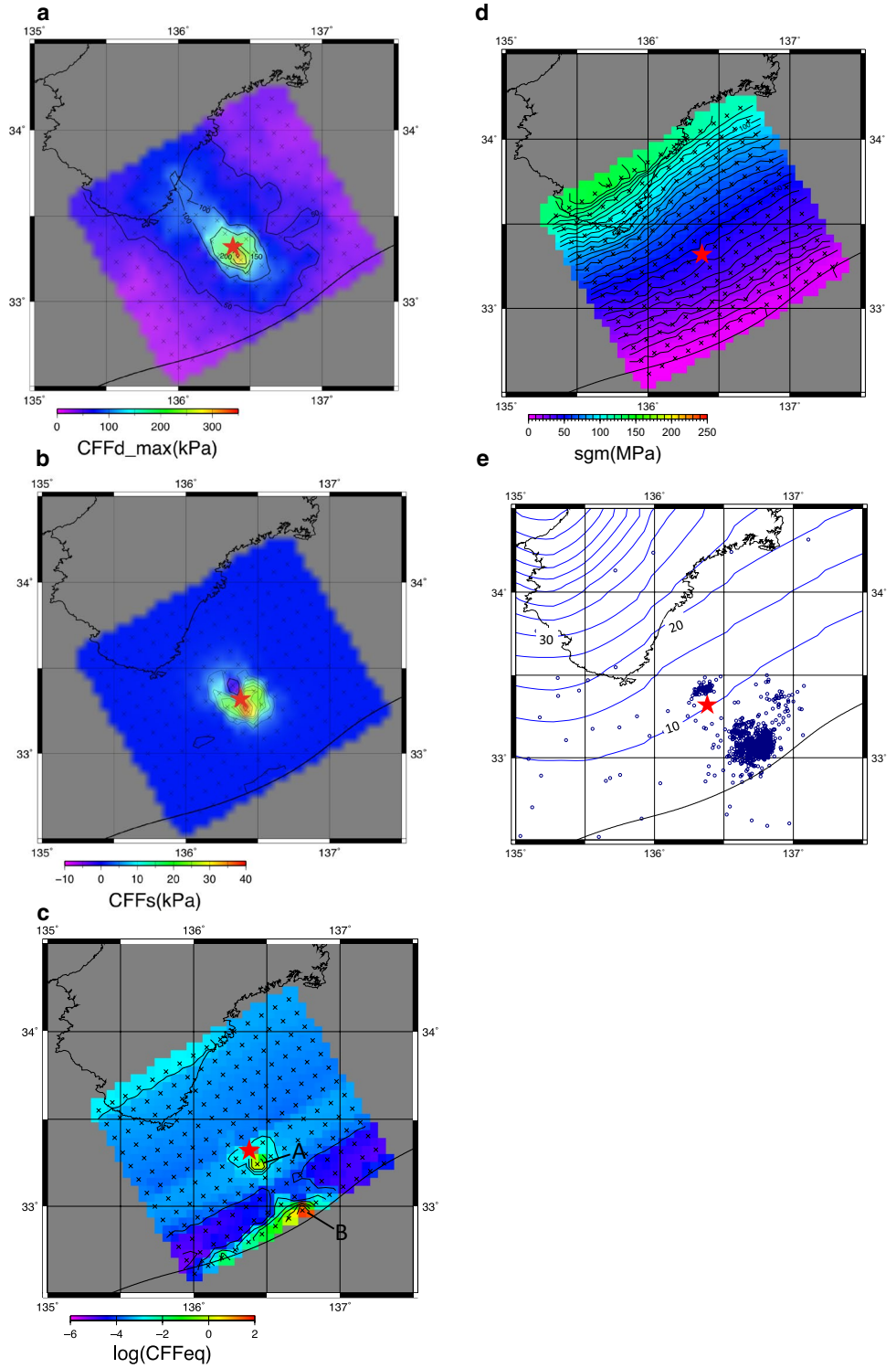

Fig. 8 Distributions of **a** CFF_{d_max}, **b** ΔCFF_s, and **c** ΔCFF_{eq} due to the 2016 Mie offshore earthquake. The red star symbol shows the epicenter of the 2016 Mie offshore earthquake. **d** Distribution of the effective normal stress. **e** The hypocenters of the low-frequency tremors which occurred from April 1 to April 13 determined by Araki et al. (2017). A SSE associated with these tremors was considered to be triggered by the Mie offshore earthquake. Blue contours show the depth of the plate boundary

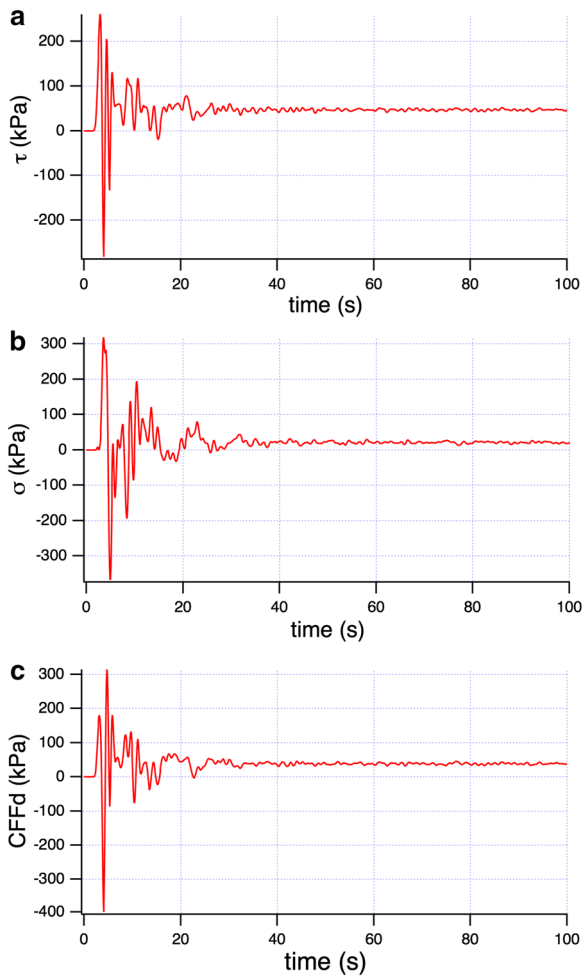

Fig. 9 Changes in **a** shear stress $\tau_d(t)$, **b** normal stress $\sigma_d(t)$, and **c** $CFF_d(t)$ due to the 2016 Mie offshore earthquake calculated at point A denoted in Fig. 8c

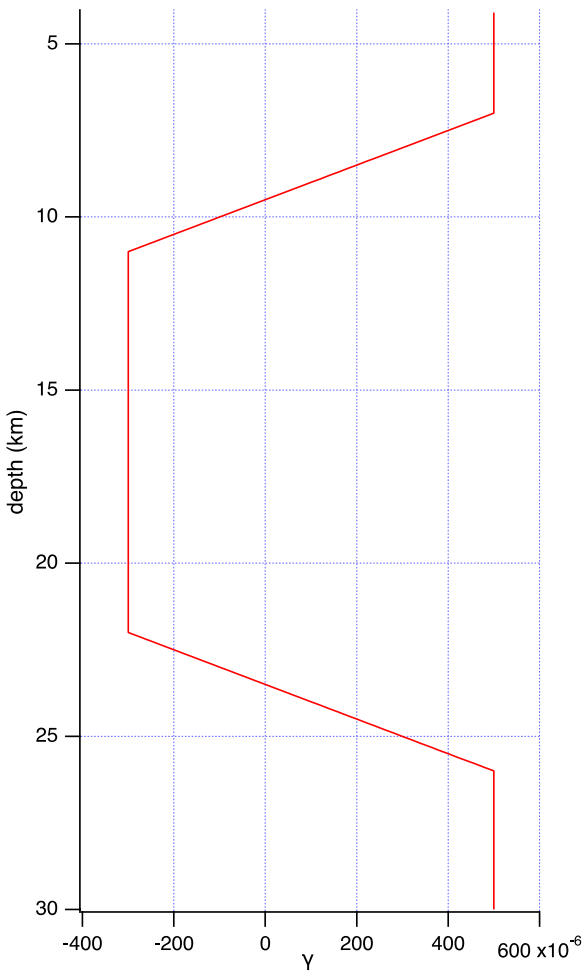

Fig. 10 Assumed variation with depth of $\gamma = a - b$

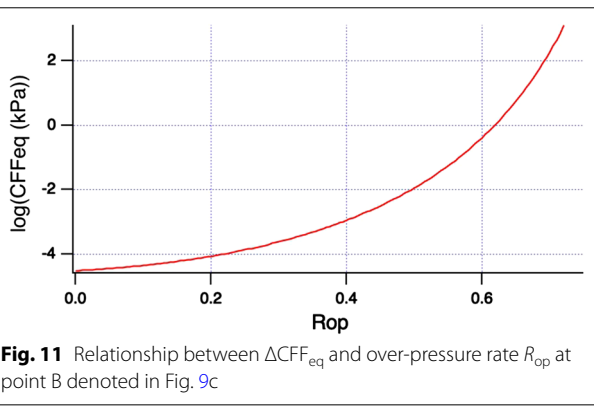

Fig. 11 Relationship between ΔCFF_{eq} and over-pressure rate R_{op} at point B denoted in Fig. 9c

shows ΔCFF_{eq} as a function of R_{OP} at point B, ΔCFF_{eq} is very sensitive to R_{OP}. This possibly explains why triggered earthquakes have been frequently observed in geothermally active or volcanic areas (e.g., Hill et al. 1993; Aiken and Peng 2014). If the pore pressure is locally very high, earthquake triggering can easily occur in such areas. Wei et al. (2018) also pointed out that low effective normal stress on the shallow subduction interface is needed to reproduce the repeating SSEs.

Discussion and summary

After the 2016 Mie offshore earthquake, shallow SSEs, shallow very low-frequency events, and shallow tremor were observed near the Nankai trough, which were probably triggered by the Mie offshore earthquake (Annoura et al. 2017; Araki et al. 2017; Nakano et al. 2018). Araki et al. (2017) reported SSEs and associated tremor swarms using data from an array of borehole and seafloor instruments. Figure 8e shows the hypocenters of the low-frequency tremors which occurred from April 1 to April 13

determined by Araki et al. (2017). They considered that a SSE accompanied by these tremors was triggered by the 2016 Mie offshore earthquake. As ΔCFF_{eq} due to the Mie offshore earthquake have large values near the trough, it may have triggered the shallow SSEs. Although the distribution of ΔCFF_{eq} shown in Fig. 8c depends on uncertain parameter values, the large ΔCFF_{eq} value near the trough was mainly caused by low effective normal stress.

The shallow region was assumed to have positive $a-b$ in the previous section. Many investigators (e.g., Du et al. 2003; Shibazaki et al. 2012; Wei et al. 2015) performed numerical simulation of SSEs assuming $a-b<0$ for the patch at the unstable–stable transient zone where SSEs occur, although Perfettini and Ampuero (2008) indicated that SSEs could occur even if $a-b>0$. If we assume a larger b resulting in $a-b<0$ in the shallow region, ΔCFF_{eq} would take a larger value in the shallow region as expected from Eq. (27). We confirmed that the ΔCFF_{eq} distribution in the shallow region is similar to that in Fig. 8c by calculating ΔCFF_{eq} assuming $a-b=\gamma_{seis}$ in the shallow region and $R_{OP}=62\%$, which is lower than the assumed value in Fig. 8c.

We proposed a normal-stress-dependent Nagata law incorporating the experimental results conducted by Linker and Dieterich (1992). Moreover, we obtained the scaling relationship for α between the aging law and the modified Nagata law was obtained (Eq. (13)). When the perturbation of normal and/or shear stress is applied, dynamic and static ΔCFF for the modified Nagata law can be calculated using Eqs. (18) or (21), respectively.

We performed numerical simulations of earthquake triggering due to static and dynamic perturbations in CFF. The triggering potentials for the static and dynamic perturbation cannot be evaluated by simply comparing CFF values. Even if the value of ΔCFF_s is smaller than the maximum value of $CFF_d(t)$, the triggering potential of the static perturbation could be higher. To compare the triggering potential of static and dynamic CFF perturbations, we derived ΔCFF_{eq} (Eq. (27)) for the dynamic case. If $\Delta CFF_s=\Delta CFF_{eq}$, both the static and dynamic perturbations have approximately the same triggering potential. On the basis of the numerical simulations, we confirmed that ΔCFF_{eq} is a good measure of the triggering potential for dynamic perturbation.

We calculated $CFF_d(t)$, ΔCFF_s, and ΔCFF_{eq} for the 2016 Mie offshore earthquake using revised OpenSWPC. ΔCFF_{eq} along the trench has large values, which may have caused the SSEs which occurred after the Mie earthquake. ΔCFF_{eq} is sensitive to the over-pressure ratio of the pore fluid. It is possible that earthquake triggering easily occurs in areas with locally high pore pressure.

Acknowledgements
We thank the editor R. Ando and two anonymous reviewers for insightful reviews. E. Araki kindly arrowed us to use the hypocenter data of the tremors. We also thank Masao Nakatani for useful suggestions. This research was supported by Japan Society for the Promotion of Science, and the Ministry of Education, Culture, Sports, Science and Technology (MEXT) of Japan, under its Earthquake and Volcano Hazards Observation and Research Program.

Authors' contributions
SY made a research plan and performed numerical simulations. TM made a new version of OpenSWPC to calculate stress tensor. NK developed the original code for the simulation, and made basic design of a new version of simulation code. All authors read and approved the final manuscript.

Funding
This research was supported by the Ministry of Education, Culture, Sports, Science and Technology (MEXT) of Japan, under its Earthquake and Volcano Hazards Observation and Research Program, and also by JSPS KAKENHI Grant Number JP18K03775.

Availability of data and materials
The OpenSWPC is an open code (https://doi.org/10.5281/zenodo.3712650).

Competing interests
The authors declare that they have no competing interests.

Author details
[1] Earthquake Research Institute, University of Tokyo, Tokyo, Japan. [2] Hirosaki University, Hirosaki, Japan.

Received: 25 March 2020 Accepted: 10 September 2020
Published online: 29 September 2020

References

Aiken C, Peng Z (2014) Dynamic triggering of microearthquakes in three geothermal/volcanic regions of California. J Geophys Res. https://doi.org/10.1002/2014JB011218

Allen CR, Wyss M, Brune JN, Grants A, Wallage RE (1972) Displacements on the Imperial, Superstition Hills, and San Andreas faults triggered by the Borrego Mountain earthquake. In: The Borrego Mountain Earthquake of April 9, 1968. Geological Survey Professional Paper. No.787

Annoura S, Hashimoto T, Kamaya N, Katsumata A (2017) Shallow episodic tremor near the Nankai Trough axis off southeast Mie prefecture, Japan. Geophys Res Lett 44:3564–3571. https://doi.org/10.1002/2017GL073006

Araki E, Saffer DM, Kopf AJ, Wallace LM, Kimura T, Machida Y, Ide S, DAavis E, IODP Expedition 365 shipboard scientists (2017) Recurring and triggered slow-slip events near the trench at the Nankai Trough subduction megathrust. Science 356:1157–1160. https://doi.org/10.1126/science.aan3120

Belardinelli ME, Bizzarri A, Cocco M (2003) Earthquake triggering by static and dynamic stress changes. J Geophys Res 108(B3):1–16. https://doi.org/10.1029/2002JB001779

Bhattacharya P, Rubin AM (2014) Frictional response to velocity steps and 1-D fault nucleation under a state evolution law with stressing-rate dependence. J Geophys Res Solid Earth 119(3):2272–2304

Bhattacharya P, Rubin AM, Bayart E, Savage HM, Marone C (2015) Critical evaluation of state evolution laws in rate and state friction: fitting large velocity steps in simulated fault gouge with time-, slip-, and stress-dependent constitutive laws. J Geophys Res Solid Earth 120:6365–6385. https://doi.org/10.1002/2015JB012437

Brodsky EE, Karakostas V, Kanamori H (2000) A new observation of dynamically triggered regional seismicity: earthquakes in Greece following the August 1999 Izmit, Turkey earthquake. Geophys Res Lett 27(17):1944–8007. https://doi.org/10.1029/2000GL011534

Canitano A, Gonzalez-Huizar H, Hsu Y-J, Lee H-M, Linde AT, Sacks S (2019) Testing the influence of static and dynamic stress perturbations on the

occurrence of a shallow, slow slip event in eastern Taiwan. J Geophys Res Earth Solid Earth 124:3073–3087. https://doi.org/10.1029/2018JB016742
Dieterich JH (1979) Modeling of rock friction: 1. Experimental results and constitutive equations. J Geophys Res 84:2161–2168
Dieterich JH (1994) A constitutive law for rate of earthquake production and its application to earthquake clustering. J Geophys Res 99:2601–2618
Dieterich JH, Cayol V, Okubo P (2000) The use of earthquake rate changes as a stress meter at Kilauea volcano. Nature 408:457–460. https://doi.org/10.1038/35044054
Du W-x, Sykes LR, Shaw BE, Scholz CH (2003) Triggered aseismic fault slip from nearby earthquakes, static or dynamic effect? J Geophys Res. https://doi.org/10.1029/2002JB002008
Gomberg J, Blanpied ML, Beeler NM (1997) Transient triggering of near and distant earthquakes. Bull Seismol Soc Am 87(2):294–309
Gomberg J, Beeler NM, Blanpied ML, Bodin P (1998) Earthquake triggering by transient and static deformations. J Geophys Res 103(B10):24411–24426. https://doi.org/10.1029/98JB01125
Hill DP, Reasenberg PA, Michael A, Arabaz WJ, Beroza G, Brumbaugh D et al (1993) Seismicity remotely triggered by the magnitude 7.3 Landers, California, earthquake. Science 260:1617–1623. https://doi.org/10.1126/science.260.5114.1617
Itaba S, Ando R (2011) A slow slip event triggered by teleseismic surface waves. Geophys Res Lett 38:L21306. https://doi.org/10.1029/2011GL049593
Johnson CW, Bürgmann R (2016) Delayed dynamic triggering: local seismicity leading up to three remote $M \geq 6$ aftershocks of the 11 April 2012 M8.6 Indian Ocean earthquake. J Geophys Res 121:134–151. https://doi.org/10.1002/2015JB012243
Kaneko Y, Lapusta N (2008) Variability of earthquake nucleation in continuum models of rate-and state faults and implications for aftershock rates. J Geophys Res 113(12):312. https://doi.org/10.1029/2007JB005154
Katakami S, Kaneko Y, Ito Y, Araki E (2020) Stress sensitivity of instantaneous dynamic triggering of shallow slow slip events. J Geophys Res Solid Earth. https://doi.org/10.1029/2019JB019178
Kato N (2004) Interaction of slip on asperities: numerical simulation of seismic cycles on a two-dimensional planar fault with nonuniform frictional property. J Geophys Res 109:B12306. https://doi.org/10.1029/2004JB003001
Kato N, Hirasawa T (1999) A model for possible crustal deformation prior to a coming large interplate earthquake in the Tokai district, central Japan. Bull Seis Soc Am 89:1401–1417
Kilb D, Gomberg J, Bodin P (2000) Triggering of earthquake aftershocks by dynamic stresses. Nature 408:570–574. https://doi.org/10.1038/35046046
Koketsu K, Miyake H, Suzuki H (2012) Japan Integrated Velocity Structure Model Version 1. In: Proceedings of the 15th World Conference on Earthquake Engineering
Lin CH (2012) Remote triggering of the M_w 6.9 Hokkaido earthquake as a result of the M_w 6.6 Indonesian Earthquake on September 11, 2008. Terr Atmos Ocean Sci 23(3):283–290. https://doi.org/10.3319/TAO.2012.01.12.01(T)
Linker MF, Dieterich JH (1992) Effects of variable normal stress on rock friction: observations and constitutive equations. J Geophys Res 97:4923–4940. https://doi.org/10.1029/92JB00017
Maeda T, Takemura S, Furumura T (2017) OpenSWPC: an open-source integrated parallel simulation code for modeling seismic wave propagation in 3D heterogeneous viscoelastic media. Earth Planets Space 69:102. https://doi.org/10.1186/s40623-017-0687-2
Miyazawa M (2011) Propagation of an earthquake triggering front from the 2011 Tohoku-Oki earthquake. Geophys Res Lett 38:L23307. https://doi.org/10.1029/2011GL049795
Miyazawa M (2016) An investigation into the remote triggering of the Oita earthquake by the 2016 Mw 7.0 Kumamoto earthquake using full wavefield simulation. Earth Planets Space 68:205. https://doi.org/10.1186/s40623-016-0585-z
Miyazawa M (2019) Bayesian approach for detecting dynamically triggered very low-frequency earthquakes in the Nankai subduction zone and application to the 2016 Mw 5.9 off-Kii Peninsula earthquake, Japan. Geophys J Int 217(2):1123–1140. https://doi.org/10.1093/gji/ggz073
Miyazawa M, Brodsky EE, Mori J (2008) Learning from dynamic triggering of low-frequency tremor in subduction zones. Earth Planets Space 60:17. https://doi.org/10.1186/BF03352858
Nagata K, Nakatani M, Yoshida S (2012) A revised rate- and state-dependent friction law obtained by constraining constitutive and evolution laws separately with laboratory data. J Geophys Res 117:B02314. https://doi.org/10.1029/2011JB008818
Nakano M, Hori T, Araki E, Kodaira S, Ide S (2018) Shallow very-low-frequency earthquakes accompany slow slip events in the Nankai subduction zone. Nat Commun 9:984. https://doi.org/10.1038/s41467-018-03431-5
Nakatani M (2001) Conceptual and physical clarification of rate and state friction: frictional sliding as a thermally activated rheology. J Geophys Res. https://doi.org/10.1029/2000JB900453
Obara K (2009) Discovery of slow earthquake families associated with the subduction of the Philippine Sea Plate in southwest Japan. Zisin 61:s315–327 **(in Japanese with English abstract)**
Parsons T, Velasco AA (2011) Absence of remotely triggered large earthquakes beyond the mainshock region. Nat Geosci 4:321–326. https://doi.org/10.1038/ngeo1110
Perfettini H, Ampuero J-P (2008) Dynamics of a velocity strengthening fault region: implications for slow earthquakes and postseismic slip. J Geophys Res 113:B09411. https://doi.org/10.1029/2007JB005398
Perfettini H, Schmittbuhl J, Cochard A (2003) Shear and normal load perturbations on a two-dimensional continuous fault: 2. Dynamic triggering. J Geophys Res 108(B9):2409. https://doi.org/10.1029/2002JB001805
Pollitz FF, Stein RS, Sevilgen V, Bu R (2012) The 11 April 2012 east Indian Ocean earthquake triggered large aftershocks worldwide. Nature 490:250–253. https://doi.org/10.1038/nature11504
Rice JR (1993) Spatio-temporal complexity of slip on a fault. J Geophys Res 98:9885–9907
Richards-Dinger K, Stein RS, Toda S (2010) Decay of aftershock density with distance does not indicate triggering by dynamic stress. Nature 467(7315):583–586. https://doi.org/10.1038/nature09402
Ruina A (1983) Slip instability and state variable friction laws. J Geophys Res 88:10359–10370
Satake K (1993) Depth distribution of coseismic slip along the Nankai Trough, Japan, from joint inversion of geodetic and tsunami data. J Geophys Res 98:4533–4565. https://doi.org/10.1029/92JB01553
Savage HM, Marone C (2008) Potential for earthquake triggering from transient deformations. J Geophys Res 113(B5):1–15. https://doi.org/10.1029/2007JB005277
Shibazaki B, Obara K, Matsuzawa T, Hirose H (2012) Modeling of slow slip events along the deep subduction zone in the Kii Peninsula and Tokai regions, southwest Japan. J Geophys Res. https://doi.org/10.1029/2011JB009083
Takemura S, Kimura T, Saito T, Kubo H, Shiomi K (2018) Moment tensor inversion of the 2016 southeast offshore Mie earthquake in the Tonankai region using a three-dimensional velocity structure model: effects of the accretionary prism and subducting oceanic plate. Earth Planets Space 70:50. https://doi.org/10.1186/s40623-018-0819-3
To A, Obana K, Sugioka H, Araki E, Takahashi N, Fukao Y (2015) Small size very low frequency earthquakes in the Nankai accretionary prism, following the 2011 Tohoku-Oki earthquake. Phys Earth Planet Inter 245:40–51. https://doi.org/10.1016/j.pepi.2015.04.007
Uchida T, Horikawa H, Nakai M, Matsushita R, Shigematsu N, Ando R, Imanishi K (2016) The 2016 Kumamoto-Oita earthquake sequence: aftershock seismicity gap and dynamic triggering in volcanic areas. Earth Planets Space 68:180. https://doi.org/10.1186/s40623-016-0556-4
van der Elst NJ, Brodsky EE (2010) Connecting near-field and far-field earthquake triggering to dynamic strain. J Geophys Res 115(B07):311. https://doi.org/10.1029/2009JB006681
van der Elst NJ, Savage HM (2015) Frequency dependence of delayed and instantaneous triggering on laboratory and simulated faults governed by rate-state friction. J Geophys Res 120:3406–3429. https://doi.org/10.1002/2014JB011611
van der Elst NJ, Brodsky EE, Lay T (2013) Remote triggering not evident near epicenters of impending great earthquakes. Bull Seis Soc Am 103(2B):1522–1540. https://doi.org/10.1785/0120120126
Wei M, Liu Y, Kaneko Y, McGuire JJ, Bilham R (2015) Dynamic triggering of creep events in the Salton Trough, Southern California by region $M \geq 5.4$ earthquakes constrained by geodetic observations and numerical simulations. Earth Planet Sci Lett 427:1–10. https://doi.org/10.1015/j.epsl.2015.06.044

Wei M, Kaneko Y, Shi P, Liu Y (2018) Numerical modeling of dynamically triggered shallow slow slip events in New Zealand by the 2016 Mw 7.8 Kaikoura earthquake. Geophys Res Lett 45:4764–4772. https://doi.org/10.1029/2018GL077879

Yoshida S (2016) Earthquakes in Oita triggered by the 2016 M7.3 Kumamoto earthquake. Earth Planets Space 68:176. https://doi.org/10.1186/s40623-016-0552-8

Yoshida S (2018) Numerical simulations of earthquake triggering by dynamic and static stress changes based on a revised friction law. J Geophys Res. https://doi.org/10.1029/2017JB014781

Yukutake Y, Miyazawa M, Honda R, Harada M, Ito H, Sakaue M, Koketsu K, Yoshida A (2013) Remotely triggered seismic activity in Hakone volcano during and after the passage of surface waves from the 2011 M9.0 Tohoku-Oki earthquake. Earth Planet Sci Lett 373:205–216. https://doi.org/10.1016/j.epsl.2013.05.004

Publisher's Note